



Densification of $\text{Sm}_{0.2}\text{Ce}_{0.8}\text{O}_{1.9}$ with the addition of lithium oxide as sintering aid

Shiru Le^{a,b}, Shengcai Zhu^c, Xiaodong Zhu^{a,b}, Kening Sun^{a,b,*}

^a State Key Laboratory of Urban Water Resource and Environment, Harbin Institute of Technology, Harbin 150090, China

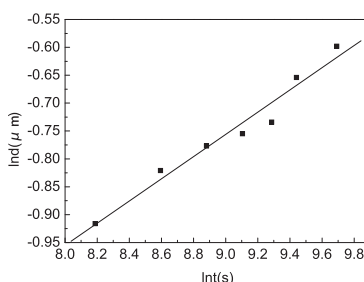
^b Natural Science Research Center, Academy of Fundamental and Interdisciplinary Sciences, Harbin Institute of Technology, Harbin, Heilongjiang 150001, China

^c Applied Chemistry Department, Harbin Institute of Technology, Harbin, Heilongjiang 150001, China

HIGHLIGHTS

- ▶ The maximum shrinkage rate of SDC was about 0.4% of that of SDC2.
- ▶ Three regions could be divided during SDC2 sintering.
- ▶ The activation energy of SDC2 was 5.54 ± 0.50 eV because of a liquid phase in grain boundary.
- ▶ The grain boundary diffusion dominant densification with $4.2 \times 10^{-17} \text{ m}^3 \text{ N}^{-1} \text{ s}^{-1}$ at 900 °C.
- ▶ The OCV of the cell using SDC2 as electrolyte is 0.78 V at 600 °C.

GRAPHICAL ABSTRACT



ARTICLE INFO

Article history:

Received 19 June 2012

Received in revised form

6 August 2012

Accepted 7 August 2012

Available online 10 September 2012

Keywords:

Solid oxide fuel cells

Samarium doped cerium oxide

Sintering aid

Mechanism

Sintering parameters

ABSTRACT

20 mol% samarium doped cerium oxide ($\text{Sm}_{0.2}\text{Ce}_{0.8}\text{O}_{1.9}$, SDC) has one of the highest ionic conductivities as electrolyte for solid oxide fuel cell in intermediate temperature, but is restricted to commercial application for its poor densification behavior. The addition of 2 mol% Li_2O in the $\text{Sm}_{0.2}\text{Ce}_{0.8}\text{O}_{1.9}$ (SDC2) improves its maximum shrinkage rate from $4.6 \times 10^{-3} \text{ min}^{-1}$ – 1.1 min^{-1} at a heating rate of $10^\circ\text{C min}^{-1}$. The relative density of SDC2 achieves 99.5% at 898 °C and 3°C min^{-1} , while it is only 82% for SDC at 1250 °C and 3°C min^{-1} . The grain boundary diffusion is the densification mechanism, and the mobility of grain boundary increases from $9.8 \times 10^{-19} \text{ m}^3 \text{ N}^{-1} \text{ s}^{-1}$ of SDC to $4.2 \times 10^{-17} \text{ m}^3 \text{ N}^{-1} \text{ s}^{-1}$ of SDC2 at 900 °C. The activation energy for densification as high as 5.5 ± 0.5 eV for SDC2 contributes to the formation of liquid phase in the grain boundary. The open circuit voltage of the cell using SDC2 as electrolyte as high as 0.78 V at 600 °C under solid oxide fuel cell (SOFC) working conditions demonstrates its promising for SOFC electrolyte.

© 2012 Elsevier B.V. All rights reserved.

1. Introduction

As one of the many materials with the potential to be used as a solid oxide fuel cell (SOFC) electrolyte at intermediate temperature of 500–700 °C, 20 mol% samarium doped cerium oxide (SDC) has one of the highest ionic conductivities [1], allowing its use in stainless steel supported fuel cells. Ceria is one of the fluorite-

structure ceramic materials and does not undergo any crystallographic transition from room temperature to its melting point in air [2]. One problem using ceria-based solid solutions as electrolytes for SOFC is their relative poor densification behavior, which requires sintering temperatures up to 1500 °C [3,4]. If a dense ceria-based electrolyte can be prepared at lower temperature, it can be co-sintered with the electrode components. This can simplify the fabrication processes and reduce the cost, helping with porous electrode microstructure control and avoiding phase diffusion and chemical interaction problems.

In order to reach complete densification, two measures are usually taken. First, the initial particles size of the powder is

* Corresponding author. Natural Science Research Center, Academy of Fundamental and Interdisciplinary Sciences, Harbin Institute of Technology, Harbin, Heilongjiang 150001, China. Tel./fax: +86 451 8641 2153.

E-mail address: keningsun@yahoo.com.cn (K. Sun).

reduced to the nanometer range, thus increasing the driving force for sintering [5,6]. However, a small pore size between ultra-fine particles produces a high capillary force in the powder compact which is the origin of low packing density and cracks formed during drying and firing [7,8]. Second, small amount of sintering aids for doped ceria has been reported in the literature [9]. Densification can be enhanced by adding small amounts of transition metal oxides, such as Mn_2O_3 [10] Fe_2O_3 [11]. In particular, Gauckler et al. [12], reported highly dense Gd doped ceria (GDC) sintered bodies with addition of Co_3O_4 .

For a dopant as a sintering aid, it must be segregated to the grain boundaries instead of dissolving in the bulk. The solubility of the dopant in CeO_2 is inversely proportional to the square of the “Vegard’s Slope” for CeO_2 [13]. The “Vegard’s Slope” of Li_2O has a value 46, demonstrating its effectiveness in being a sintering aid [14–17].

However, it is still needed to understand the sintering mechanisms of ceria-based solid solutions with sintering aids in more detail. Both the densification activation energy and mechanism, together with the mobility of the grain-boundary and the open circuit voltage of the cell using the electrolyte with sintering aid under fuel cell working conditions, all these are still unclear. In the present work, the processes of densification and grain growth of $\text{Sm}_{0.2}\text{Ce}_{0.8}\text{O}_{1.9}$ with 2 mol % Li_2O as a sintering aid were investigated, and important sintering parameters were determined. Based on the achieved results, the changes of relative density, grain size, and shrinkage rate with sintering temperature were revealed. The activation energy for densification was determined. The sintering mechanism was explored and the grain boundary mobility was calculated. The open circuit voltages (OCV) of the cell using the SDC2 under SOFC working condition were evaluated as well.

2. Experimental

The $\text{Ce}_{0.8}\text{Sm}_{0.2}\text{O}_{1.9}$ powder was prepared by co-precipitation method. Cerium and samarium nitrate hexahydrate (>99.99%, Beijing Faounde Star Co., China) were used as starting materials. Ammonia (25 wt%, A.R., China) was employed as precipitants. The mental nitrate solution was dropped into the ammonia solution, which pH was held at 9 under stirring. Then the precipitate was filtered, rinsed with water and ethanol for three times. At last, the powders were dried at 90 °C for 24 h then calcined at 600 °C for 2 h.

The $\text{Ce}_{0.8}\text{Sm}_{0.2}\text{O}_{1.9}$ powders with and without 2 mol % Li_2O as sintering aid was noted as SDC and SDC2, respectively. Then the powders were milled in a planetary ball mill for 24 h. These powders were pressed at 300 MPa into pellets of $\Phi 20$ mm with 0.8 mm in thickness. After that, the pellets were sintered in air from room temperature to required temperature at 3 K min^{−1}.

A horizontal push-rod dilatometer (DIL 402PC Netzsch, Germany) was used for monitoring the in-situ shrinkage in the axial direction of the samples during sintering. A slight load of 40 cN was exerted on the sample so as to minimize the external effect of too high load. Three heating rates of 3 K min^{−1}, 5 K min^{−1} and 10 K min^{−1} were used. The accuracy of the measurement was within ± 0.1 μm . Before the sample measurement, baselines were created using Netzsch Al_2O_3 as a standard with the identical heating profile so that instrument length variation could be calibrated. The instantaneous relative density was calculated by the equation [18].

$$\rho = \rho_0 \left(1 + \frac{dL}{L} \right)^3 \quad (1)$$

Here dL/L was the instantaneous shrinkage in percentage, ρ was the actual relative density and ρ_0 was the green density.

The crystal structures of the as-prepared powders were characterized by X-ray diffraction (XRD, Cu K α radiation wavelength $\lambda = 1.5405$ Å). The Brunauer–Emmett–Teller (BET) specific surface area was obtained via N_2 adsorption at 77 K (Micromeritics, ASAP 2020, USA).

The microstructures and morphologies of the prepared powders and sintered bodies were determined using a field emission-scanning electron microscope (FESEM, Hitachi S4800). The average grain size was calculated from the SEM images. To evaluate the OCV of the cell using SDC2 as electrolyte, the SDC2 sample was pasted with Pt slurry and connected with Ag wire as current collector. Then the cell was sealed by glass in an alumina oxide tube. The performance of cells was measured by Arbin Instruments, using H_2 with 3% H_2O as fuel at a flow rate of 100 ml min^{−1} and air as oxidant.

3. Sintering model

Herring’s scaling law is based on the idea that particles remain geometrically identical during sintering besides a change in scale [19]. Starting from Herring’s general flux equation, the total atomic flux is expresses as follows.

$$-\frac{dL}{Ldt} = \frac{\gamma\Omega}{RT} \left[\frac{\Gamma D_0}{d^n} \exp\left(\frac{-Q}{RT}\right) \right] \quad (2)$$

Here, γ the surface energy, Ω is the atomic volume, and δ the grain boundary thickness, L is the actual length, d is the actual grain size, R is the Boltzmann constant, T is the current temperature, and Q is the activation energy. The value of Γ is a collection of scaling factors that relate features such as the diffusion distance or the grain boundary area of the microstructure to the grain size at any given instant. The value of n is specific to the dominant diffusion mechanism. For the grain boundary diffusion, $n = 4$; for volume diffusion, $n = 3$. Rearranging and taking the logarithm on both sides of Eq. (2) yields the following equation:

$$\ln\left(-\frac{dL}{Ldt}\right) = \ln\left(\frac{\gamma\Omega\Gamma D_0}{RT}\right) - n\ln d - \frac{Q}{RT} \quad (3)$$

The activation energy of the densification can be determined by simply plotting the term on the left-hand side of Eq. (3) versus $1/T$ at a constant relative density for different heating rates [18]. The slope of the obtained straight line equals $-Q/R$.

Conversely, at an isothermal sintering temperature, $\gamma\Omega\Gamma D_0/RT$, Q/RT and dL/Ldt change little and could be considered nearly as a constant. Then d^n is the function of time [20].

$$d^n = F(t) + \text{constant} \quad (4)$$

By integrating Eq. (4), one can obtain

$$d^{n+1} - d_0^{n+1} \approx F(t - t_0) \quad (5)$$

where F is a constant related to grain growth and t_0 is the starting sintering time of the isothermal sintering, which is 0 in this work. As the isothermal sintering proceeds, d_0^{n+1} becomes incremental small compared to d^{n+1} and thus d_0^{n+1} can be neglected after a period of sintering time. Taking the logarithm of both sides, one can obtain [20]

$$\ln d \approx \frac{1}{n+1} \ln t + \frac{1}{n+1} \ln F \quad (6)$$

Using the relationship between the grain size and sintering time obtained from the equation, n could be calculated.

4. Results and discussion

The equivalent particle size of the powder calcined at 600 °C was obtained indirectly through XRD pattern in Fig. 1. The crystallite size was calculated to be 6.0 nm by the X-ray line broadening technique performed on the (111) diffraction peak. The BET specific surface area was 125.0 m² g^{−1} and the corresponding equivalent particle size was 6.7 nm by assuming a spherical particle shape. The morphology of typical SDC powder was shown in Fig. 2. A homogenous secondary particle of about 30 nm was achieved.

Fig. 3 exhibited the grain size evolution of SDC and SDC2 at a heating rate of 3 °C min^{−1}. The average grain size of SDC2 kept no obvious change when the density was lower than 82 % at 700 °C, but it increased rapidly thereafter as the relative density increased. It reached 0.35 μm at 950 °C. Conversely, the grain size of SDC was kept nearly no change when the relative density was lower than 70% at 700 °C, then it increased after that. It reached 0.22 μm when it was sintered at 1300 °C with the relative density only 82%. The result of increasing average grain size of the sample with sintering aid at a relative density about 82 % was consistent with cobalt oxide doped GDC [18]. Z. He [20] also reported that a small increase of grain size for GDC in a reducing atmosphere when the relative density was lower than 85% and then increased rapidly thereafter.

Fig. 4 and Fig. 5 showed the shrinkage and shrinkage rate of the SDC and SDC2 sintered at various heating rates. The maximum shrinkage rate increased as the heating rate increased. These were ascribed to a prolonged time scale for mass transport and diffusion when a slower heating rate was used to reach the same temperature [21]. It can be noted that nearly full density was obtained at about 900 °C for the SDC2 in Fig. 5, while it was only 81.5% for the SDC in Fig. 4. 900 °C was much lower for SDC to achieve fully density of 1500 °C and it was suggested it may be possible to produce a metal supported SOFC at temperatures below the 1000 °C currently used [22]. In addition, the maximum shrinkage rate was 1.1 min^{−1} for the SDC2 at 10 °C min^{−1}, while it was only 4.6 × 10^{−3} min^{−1} for SDC, which was only about 0.4 % of that of SDC2. This demonstrated that the effect of lithium oxide as sintering aid was evident.

Fig. 5(a) indicated that the SDC2 achieved a density of 99.5% at 898 °C and 3 °C min^{−1}, 953 °C and 5 °C min^{−1}, 1048 °C and 10 °C min^{−1}, respectively. In the case of SDC, a density of only 82% was achieved even sintered at 1250 °C, regardless of its heating rate. The effect of lithium oxide doping is clearly visible. The start of sintering was brought forward with lithium oxide addition. For

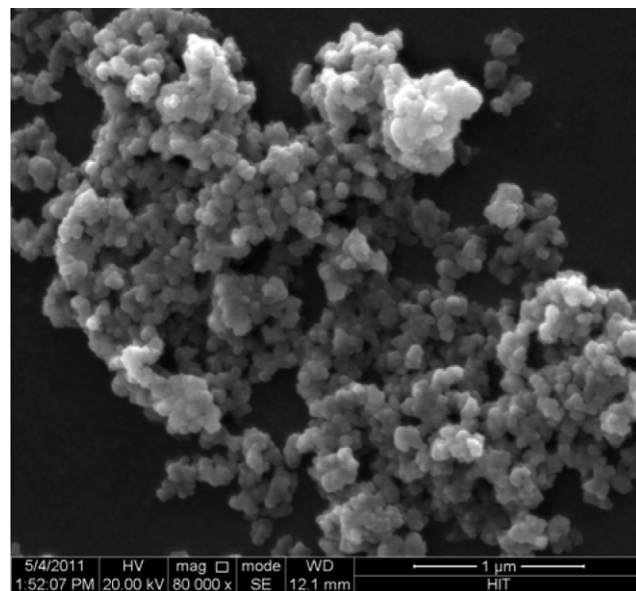


Fig. 2. SEM image of the SDC powder calcined at 600 °C.

example, at a heating rate of 5 °C min^{−1}, the start of sintering was brought forward from 600 °C to 500 °C. This was possible that gradient in the chemical potential between the particle neck and the surface increased as this addition of lithium oxide, thus increased the flux of the CeO₂ atoms [12].

From Fig. 5(a) and (b), it could be readily seen that three regions could be recognized divided: a slowly increasing density region at temperature lower than 500 °C, an intermediate region with a steep increase of density in a temperature range of 500 °C to 850 °C, and a third region at large particle size with a slower increase in density when the temperature was higher than 850 °C. The main process in region I was that of homogenization and stochastic particle relocation. Coarsening at this stage is correlated to homogenization and relocation but not densification. This was consisted with the grain size evolution in Fig. 3. The main process in region II is repacking. Densification proceeded by particle repacking, which is motivated by coarsening. Densification in region III is controlled by grain boundary diffusion, which is confirmed by the later part.

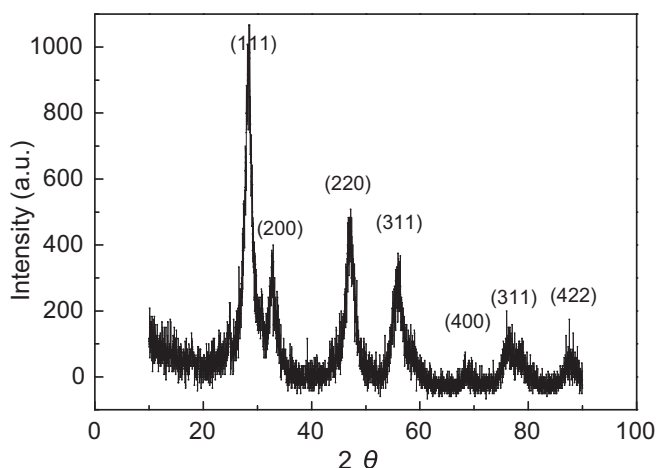


Fig. 1. XRD pattern of the SDC powder calcined at 600 °C.

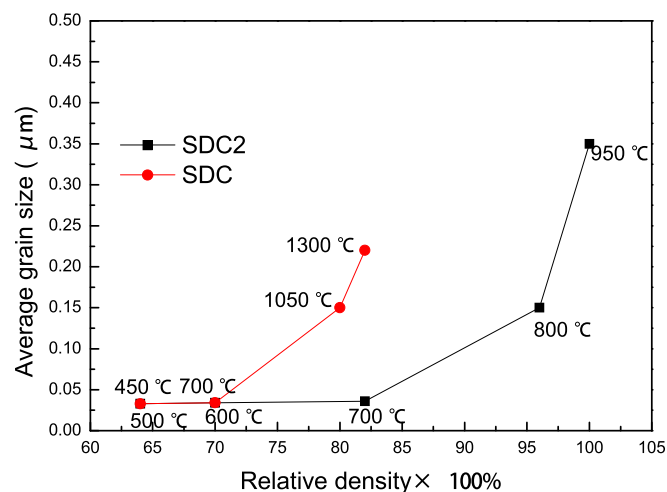


Fig. 3. Grain size evolution of SDC and SDC2 during sintering at a heating rate of 3 °C min^{−1}.

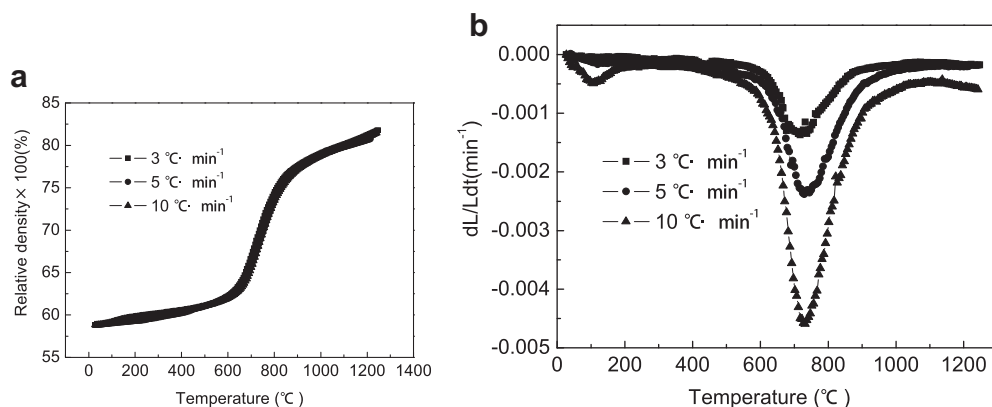


Fig. 4. Constant heating rate sintering of SDC (a) Relative density as a function of temperature, (b) Shrinkage rate as a functional of temperature.

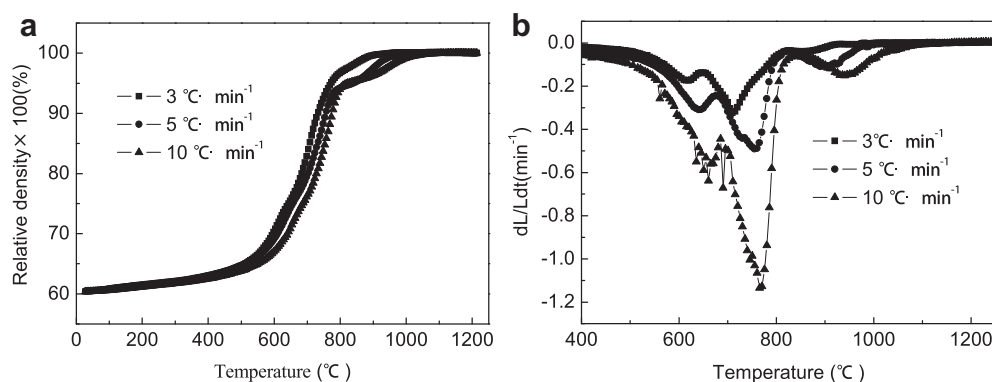


Fig. 5. Constant heating rate sintering of SDC2 (a) Relative density as a function of temperature, (b) Relative shrinkage rate as a functional of temperature.

The activation was determined from the slope of the line at various heating rate at the same relative density [18,23]. To calculate the densification activation energy, five different specific relative densities (70%, 75%, 80%, 85%, 90%) and three heating rate ($3^{\circ}\text{C}\cdot\text{min}^{-1}$, $5^{\circ}\text{C}\cdot\text{min}^{-1}$ and $10^{\circ}\text{C}\cdot\text{min}^{-1}$) had been considered. The results were shown in Fig. 6. The activation energy of SDC2 remained somewhat constant in the analyzed density regime. The calculated activation energy was 5.54 ± 0.50 eV for SDC2. This was

higher than that of 4.70 ± 0.32 eV for pure GDC reported by Jud [18], although the addition of lithium oxide lead to a lower sintering temperature and higher shrinkage rate. Increased activation energies for densification because of doping has been observed in several sintered materials, notably in TiO_2 and ZrO_2 doped Al_2O_3 [23], and Fe doped CeO_2 [24]. The higher activation energy could be assigned to the presence of a liquid phase in grain boundary. Evidence of a grain boundary phase in the SEM image was shown in Fig. 7, in which SDC2 pellet was sintered at 900 $^{\circ}\text{C}$ and 1200 $^{\circ}\text{C}$ for 2 h, respectively. The SDC grains were spherical and well dispersed, covered by the solidified melted phase. A second phase was detected at the grain boundary.

The TG-DTA curves of the Li_2O in air atmosphere are shown in Fig. 8. The TG curve showed that there were two small increase plateaus in temperature range of 50 $^{\circ}\text{C}$ and 700 $^{\circ}\text{C}$, which was because the adsorption of carbon dioxide to lithium oxide [25]. The endothermic peak of 420 $^{\circ}\text{C}$ was contributed to the melt of Li_2O [26] while the endothermic peaks in temperature range of 686 $^{\circ}\text{C}$ –710 $^{\circ}\text{C}$ corresponds to the decomposition of lithium carbonate to lithium oxide [16]. Therefore, the solidified melted phase is lithium oxide. The ceria grain was covered by solidified melted phase was also found in the SDC with molten LiNO_3 additive [9]. Zhang et al. [27] observed that CoO_{1-x} particles precipitate on the grain boundary for a cobalt-oxide-doped GDC.

The variation of logarithm of grain size when the samples were sintered at 800 $^{\circ}\text{C}$ with logarithm of sintering time was shown in Fig. 9. A linear fit was obtained. The value of n was 4 and F was $3.01 \times 10^{-6} \mu\text{m}\cdot\text{s}^{-1}$, respectively. The determined n of 4 corresponded to grain boundary diffusion dominant densification. This was because the liquid phase in the grain boundary area greatly

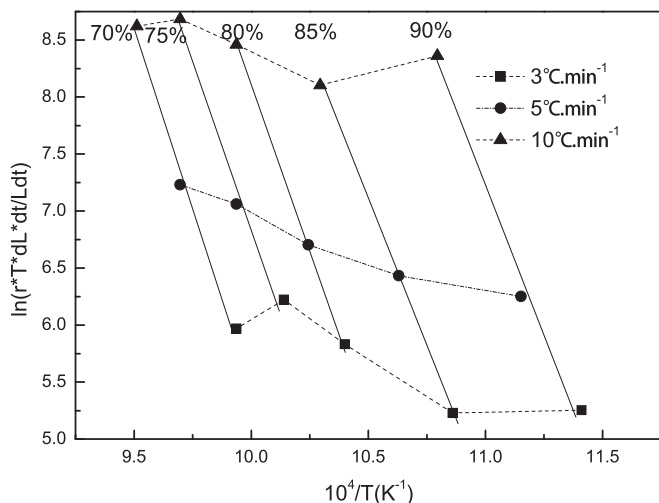


Fig. 6. The determination of the activation energy.

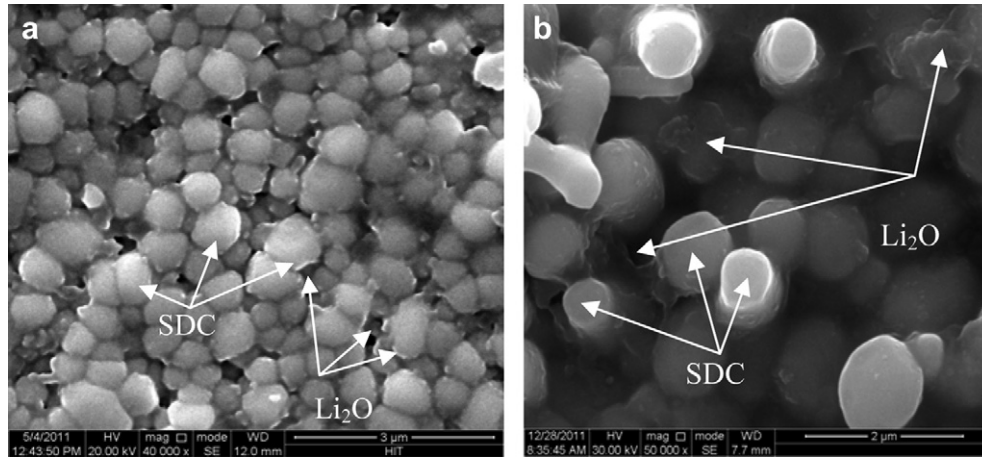


Fig. 7. The SEM image of the SDC2 sintered at 900 °C (a) and 1200 °C(b).

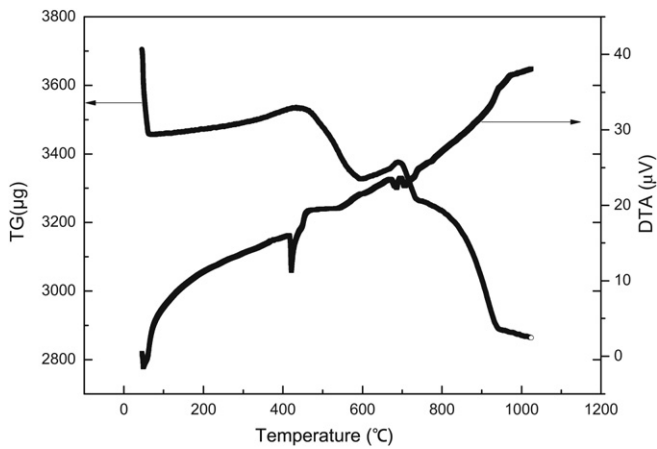


Fig. 8. TG-DTA analysis of Li_2O in air at a heating rate of $5\text{ }^\circ\text{C min}^{-1}$.

increased the flux of atoms along the grain boundary. Chen and Chen [5,6] reported that grain-boundary diffusion was the dominant densification mechanism for pure ceria, while Jud [18] reported that both grain boundary diffusion and lattice diffusion governed the densification of cobalt oxide doped GDC20.

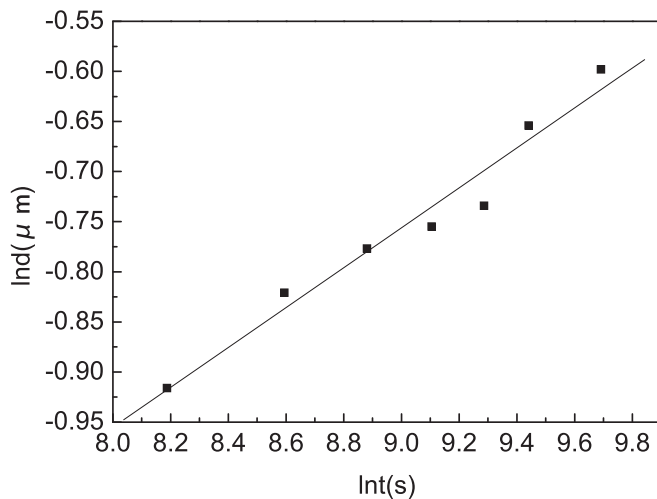


Fig. 9. Variation of logarithm of grain size with logarithm of sintering time of SDC2 sintered at 800 °C.

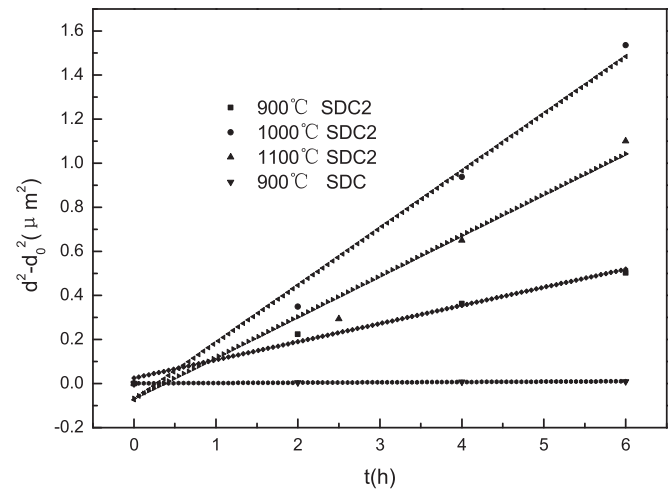


Fig. 10. Grain growth kinetics of SDC and SDC2.

Mobility of grain boundary M , can be estimated from the grain growth kinetics via the following equation [28].

$$d^2 - d_0^2 = 2M\gamma(t - t_0) \quad (7)$$

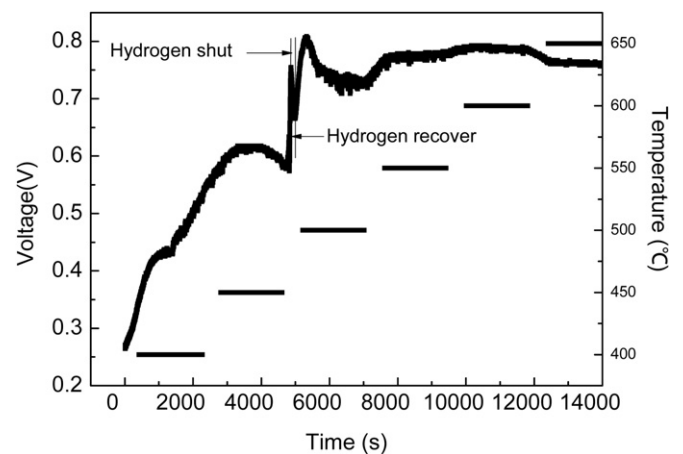


Fig. 11. The OCV of the cell using SDC2 as electrolyte under SOFC operating conditions.

In the above, d is the average grain size at time t , d_0 is the reference grain size at time t_0 , and γ is the grain boundary energy. To avoid the influence of porosity on grain boundary mobility, the temperature of higher than 900 °C was chosen to achieve the relative density as high as achieved 99%. The γ varied by no more than a factor of two over a wide range of temperature, compositions, and even grain boundary structures within the same system. Therefore, it is assumed that γ remains constant at an estimated value of 0.3 J m^{-2} and evaluated the mobility from the slope directly. This allowed us to compute the grain boundary mobility with and without Li_2O as sintering aid in the SDC systems with reasonable certainty. Fig. 10 demonstrated that the mobility of grain boundary improved rapidly. It was clear that the relationship between $d^2 - d_0^2$ and $t - t_0$ was linear. It was apparent that the value of the slope varied over several orders of magnitude. It was $4.2 \times 10^{-17} \text{ m}^3 \text{ N}^{-1} \text{ s}^{-1}$ at 900 °C, $7.5 \times 10^{-17} \text{ m}^3 \text{ N}^{-1} \text{ s}^{-1}$ at 1000 °C, $1.1 \times 10^{-16} \text{ m}^3 \text{ N}^{-1} \text{ s}^{-1}$ for SDC2, compared with that of $9.8 \times 10^{-19} \text{ m}^3 \text{ N}^{-1} \text{ s}^{-1}$ for SDC at 900 °C.

To apply SDC2 as electrolyte for SOFC, the OCV of the cell using SDC2 as electrolyte is an important value. The changes of the OCV of the cell using SDC2 as electrolyte with hydrogen in the anode side and air in the cathode side were shown in Fig. 11. It could be seen that the OCV increased slowly as the hydrogen flow proceed. A rapidly increase of OCV appeared when the time was about 4700 s. The OCV decreased with a shut of hydrogen supply, and then recovered when the hydrogen supplied again. After a fluctuation for 2300 s, the OCV was kept stable at 0.78 V at 600 °C and 0.76 V at 650 °C. Compared with that of 0.83 V at 600 °C [29] for SDC as electrolyte, the small lower OCV of SDC2 was contributed to the reduction of lithium oxide to lithium at high temperature, which lead to electronic conductivity. The OCV of SDC2 as high as 0.78 V at 600 °C demonstrated its promising as SOFC electrolyte under SOFC working conditions.

5. Conclusions

The present work focused on the investigation of the densification processes and grain growth of SDC with 2 mol% lithium oxide as the sintering aid. The grain size increased rapidly when the relative density was higher than 82%. The maximum shrinkage rate of SDC was only about 0.4% of that of SDC2. The relative density of SDC2 achieved 99.5% at 900 °C and $3 \text{ °C} \cdot \text{min}^{-1}$, while it was only 82% for SDC even at 1250 °C. The activation energy for densification as high as $5.54 \pm 0.50 \text{ eV}$ for SDC2 contributed to the formation of liquid phase in the grain boundary. The grain boundary diffusion dominated the densification processes and the grain boundary mobility was $4.2 \times 10^{-17} \text{ m}^3 \text{ N}^{-1} \text{ s}^{-1}$ at 900 °C, while it was only $9.8 \times 10^{-19} \text{ m}^3 \text{ N}^{-1} \text{ s}^{-1}$ for SDC at the same temperature. The OCV

changes of the cell using SDC2 as electrolyte under SOFC working conditions was kept stable at 0.78 V at 600 °C, demonstrating its promising for SOFC electrolyte.

Acknowledgment

This work was supported by Open Project of State Key Laboratory of Urban Water Resource and Environment, Harbin Institute of Technology (No.QA201119). Natural Scientific Research Innovation Foundation in Harbin Institute of Technology Project (HIT.NS-RIF.2009078), National Scientific Foundation of China (No.21006016), Specialized Research Fund for the Doctoral Program of Higher Education of China (20102302120044) and Postdoctoral Science-Research Foundation (LBH-Q11112).

References

- [1] Y.F. Zheng, M. Zhou, L. Ge, S.J. Li, H. Chen, L.C. Guo, *J. Alloys Compd.* 509 (2011) 546–550.
- [2] D.D. Matvei Zinkevich, Fritz Aldinger, *Solid State Ionics* 177 (2006) 989–1001.
- [3] F. Krok, I. Abrahams, W. Wrobel, A. Kozanecka-Szmigiel, J.R. Dygas, *Mater. Sci. Poland* 24 (2006) 13–22.
- [4] S.L. Reis, E.C.C. Souza, E.N.S. Muccillo, *Solid State Ionics* 192 (2011) 172–175.
- [5] P.L. Chen, I.W. Chen, *J. Am. Ceram. Soc.* 79 (1996) 3129–3141.
- [6] P.L. Chen, I.W. Chen, *J. Am. Ceram. Soc.* 80 (1997) 637–645.
- [7] T.S. Zhang, P. Hing, H.T. Huang, J. Kilner, *J. Mater. Process. Technol.* 113 (2001) 463–468.
- [8] J.S. Lee, K.O. Choi, B.K. Ryu, B.C. Shin, I.S. Kim, *Ceram. Int.* 30 (2004) 807–812.
- [9] V. Esposito, M. Zunic, E. Traversa, *Solid State Ionics* 180 (2009) 1069–1075.
- [10] T.S. Zhang, L.B. Kong, Z.Q. Zeng, H.T. Huang, P. Hing, Z.T. Xia, J. Kilner, *J. Solid State Electrochem.* 7 (2003) 348–354.
- [11] E.S. Masashi Mori, Bernard Pacaud, Keiichi Mura, Toshihiro Moriga, *J. Power Sources* 157 (2006) 688–694.
- [12] C. Kleinlogel, L.J. Gauckler, *Adv. Mater.* 13 (2001) 1081–1085.
- [13] D.J. Kim, *J. Am. Ceram. Soc.* 72 (1989) 1415–1421.
- [14] J.D. Nicholas, L.C. De Jonghe, *Solid State Ionics* 178 (2007) 1187–1194.
- [15] M.Z. Vincenzo Esposito, Enrico Traversa, *Solid State Ionics* 180 (2009) 1069–1075.
- [16] S. Li, C. Xian, C. Sun, Z. Wang, L. Chen, *J. Power Sources* 205 (2012) 57–62.
- [17] M. Han, Z. Liu, S. Zhou, L. Yu, *J. Mater. Sci. Technol.* 27 (2011) 460–464.
- [18] C.B.H. Eva Jud, Ludwig J. Gauckler, *J. Am. Ceram. Soc.* 88 (2005) 3013–3019.
- [19] C. Herring, *J. Appl. Phys.* 21 (1950) 301–303.
- [20] H.Y. Zeming He, Julie Anne Glasscock, Christodoulos Chatzichristodoulou, John William Phair, Andreas Kaiser, Severine Ramousse, *Acta Mater.* 58 (2010) 3860–3866.
- [21] X. Song, J. Lu, *J. Am. Ceram. Soc.* 94 (2011) 1053–1059.
- [22] D.C.N.P. Brandon, D. Cummins, A. Duchett, K. El-Khoury, D. Haigh, R. Leah, G. Lewis, N. Maynard, T. McColm, R. Trezona, A. Selcuk, M. Schmidt, *J. Mater. Eng. Perform.* 13 (2004) 253–256.
- [23] R.R. Jenqdwang Wang, *J. Am. Ceram. Soc.* 73 (1990) 1172–1175.
- [24] T.S. Zhang, P. Hing, H.T. Huang, J. Kilner, *J. Mater. Sci.* 37 (2002) 997–1003.
- [25] X.S. Yin, S.P. Li, Q.H. Zhang, J.G. Yu, *J. Am. Ceram. Soc.* 93 (2010) 2837–2842.
- [26] Yu Baoyu, *Rare Metals* 02 (1992) 98–101.
- [27] W.S. Zaoli Zhang, Manfred Ruhle, Eva Jud, Ludwig J. Gauckler, *Acta Mater.* 55 (2007) 2907–2917.
- [28] I.W.C. Pei, Lin Chen, *J. Am. Ceram. Soc.* 79 (1996) 1793–1800.
- [29] X. Fang, G. Zhu, C. Xia, X. Liu, G. Meng, *Solid State Ionics* 168 (2004) 31–36.